X-ray CCD Calibration for the AXAF CCD Imaging Spectrometer

M. Bautz, S. Kissel, G. Prigozhin, S. Jones, T. Isobe,
H. Manning, M. Pivovaroff, G. Ricker and J. Woo[1]
Massachusetts Institute of Technology Center for Space Research, Cambridge, MA 02139

ABSTRACT

We summarize the strategy and techniques used to calibrate X-ray CCD detectors for the AXAF CCD Imaging Spectrometer in the spectral range between 0.2 keV and 10 keV. The very demanding calibration requirements (energy scale knowledge error of order 0.1%; detection efficiency knowledge error of order 1%) are reviewed. The primary standards chosen for the calibration are discussed, with particular attention to the use of undispersed synchrotron radiation as a primary radiometric standard for the detection efficiency calibration. We review the basic models of the detector response which it is the objective of the calibration enterprise to constrain. The accuracy and reproducibility of the energy scale, spectral redistribution and detection efficiency calibration is discussed and illustrated with sample results from calibration of flight detectors.

Keywords: X-rays, charge coupled devices (CCD), calibration, AXAF, ACIS

1 INTRODUCTION

The Advanced X-ray Astrophysics Facility (AXAF), scheduled for launch in 1998,[1] will provide high-angular-resolution imaging spectroscopy and transmission grating spectroscopy in the 0.1-10 keV band. We, together with colleagues at the MIT Lincoln Laboratory and the Pennsylvania State University, are developing the AXAF CCD Imaging Spectrometer (ACIS), one of AXAF'S two focal plane scientific instruments.[2] ACIS employs X-ray-photon-counting CCDs designed and produced at MIT Lincoln Laboratory.[3] AXAF scientific objectives call for extremely accurate knowledge of instrumental response; for example, the goal for detection efficiency knowledge accuracy is of order 1%, and the corresponding goal for energy scale knowledge is of order 0.1%.

Even to approach these calibration goals, which are unprecedented in X-ray astronomy, requires an extensive, carefully planned calibration program. ACIS calibration, itself a subset of the AXAF Observatory calibration effort, will occur in several phases. In this paper, we describe the first and most time consuming phase of ACIS calibration, in which individual CCD detectors are calibrated before they are installed in the instrument. ACIS flight detector calibration has been underway since early this year, and a complete set of calibration data has been acquired for some fifteen devices. We believe we have acquired data which will meet or nearly meet each of our ambitious calibration goals. Our objective here is to describe the overall calibration approach and to present sample results which illustrate the quality of the data. A series of companion papers [4–7] describe various aspects of the instrumentation and analysis tools developed to implement the calibration plan.

Following a brief description of the ACIS instrument in section 2, we discuss the calibration strategy in section 3. In sections 4 and 5 we describe the objectives, measurements and selected preliminary results of our program to determine the CCD spectral response function and detection efficiency.

[1] Current Address: Harvard-Smithsonian Center for Astrophysics, 60 Garden Street, Cambridge, MA 02138

2 The ACIS Instrument

The ACIS focal plane contains ten MIT Lincoln Laboratory CCID17 detectors. The CCID17 is a three-phase, frame transfer imager with 1026 rows of 1024 columns in each of the imaging and framestore areas. The pixels in the imaging area are 24 microns square. The device is served by four output nodes which are (usually) operated in parallel. ACIS flight detectors are fabricated of high-resistivity silicon ($\rho > 6500\Omega - cm$) to maximize depletion depth and, therefore, high-energy X-ray detection efficiency. Flight CCDs have been fabricated in both front-illuminated and back-illuminated configurations. In this paper, we confine our discussion to the front-illuminated devices.

The engineering model ACIS focal plane is shown in Figure 1. The focal plane consists of ten detectors, organized into two arrays. The devices in the 2-chip-by-2 chip ACIS-I array are intended primarily for high-angular resolution, wide-field imaging, and are therefore tilted to conform as nearly as possible to the highly-curved focal surface of the AXAF High-Resolution Mirror Assembly. The linear, 6-chip-long ACIS-S array is intended primarily for use with the AXAF High-energy Transmission Gratings (HETG) .[8] The ACIS-S detectors are oriented to conform to the Rowland circle of the HETG. The gaps between adjacent CCDs are typically 300 microns wide, and are in no case more than 500 microns wide. In orbit, the focal plane is radiatively cooled to a temperature of -120 C. This relatively low temperature minimizes the sensitivity of the detectors to damage from energetic protons encountered on-orbit.

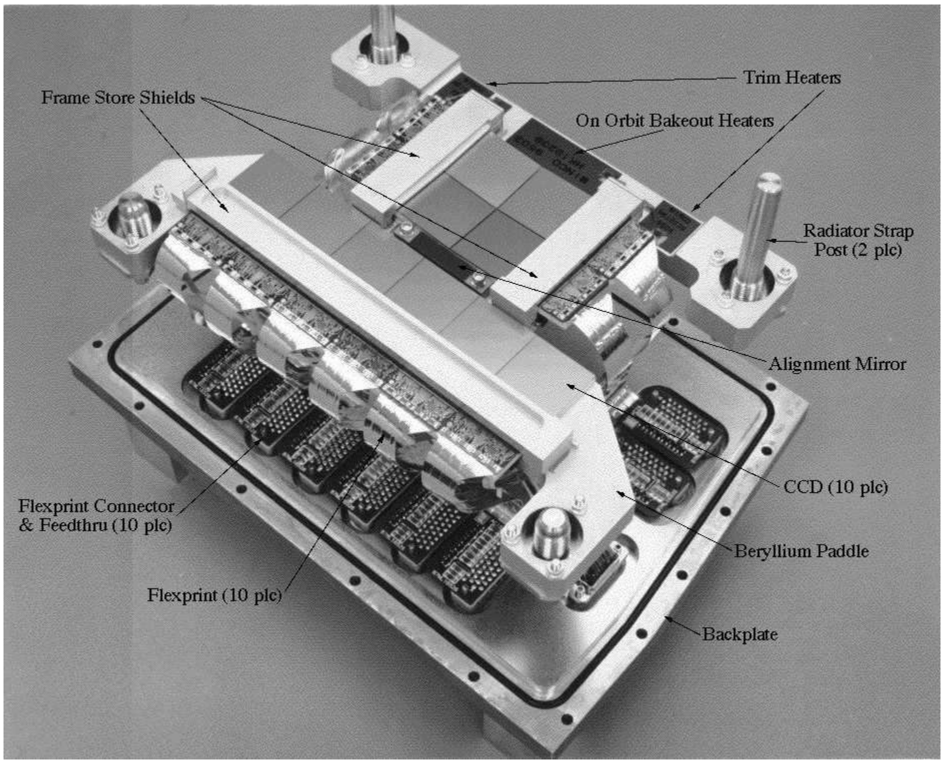

Figure 1: The ACIS CCD focal plane. The ten CCD detectors are arranged in two subarrays. The 2-by-2 detector subarray supports wide-field imaging. The 1-by-6 detector subarray supports transmission grating spectroscopy and narrow-field imaging. The engineering model is shown here; the flight detector configuration is identical.

The ACIS focal plane is served by a low-noise ($< 2e^-$ RMS) detector electronics assembly which contains a dedicated signal chain for each of the 40 CCD output nodes in the focal plane. Each signal chain operates at a rate of 100 kpixels s^{-1}, allowing a full detector readout in less than 3 seconds. The clock sequences produced by the detector electronics are programmable, so a variety of CCD readout modes are available.

Raw digital data from the detector electronics passes to a high-throughput digital processing assembly which can service as many of six operating CCDs simultaneously. The digital processing hardware and software determine the CCD bias (energy zero-point) level on a pixel by pixel basis, extract X-ray event information from the incoming data stream, and format and buffer that data for telemetry to the ground.

ACIS requires optical blocking filters to reject out-of-band radiation (mainly optical and UV light). Calibration of these filters, which is a critical part of the ACIS calibration program, is described elsewhere.[9,10]

3 Calibration Strategy

The fundamental purpose of the scientific calibration of AXAF is to develop accurate predictions of the system response (in engineering units) to any scientifically interesting X-ray flux distribution. The basic strategy adopted to achieve this end is to develop physical performance models of each of the Observatory's scientific subsystems, and to constrain and verify these models by well-chosen ground measurements. The subsystem (telescope, grating and detector) models are then to be checked during calibration of the integrated system.

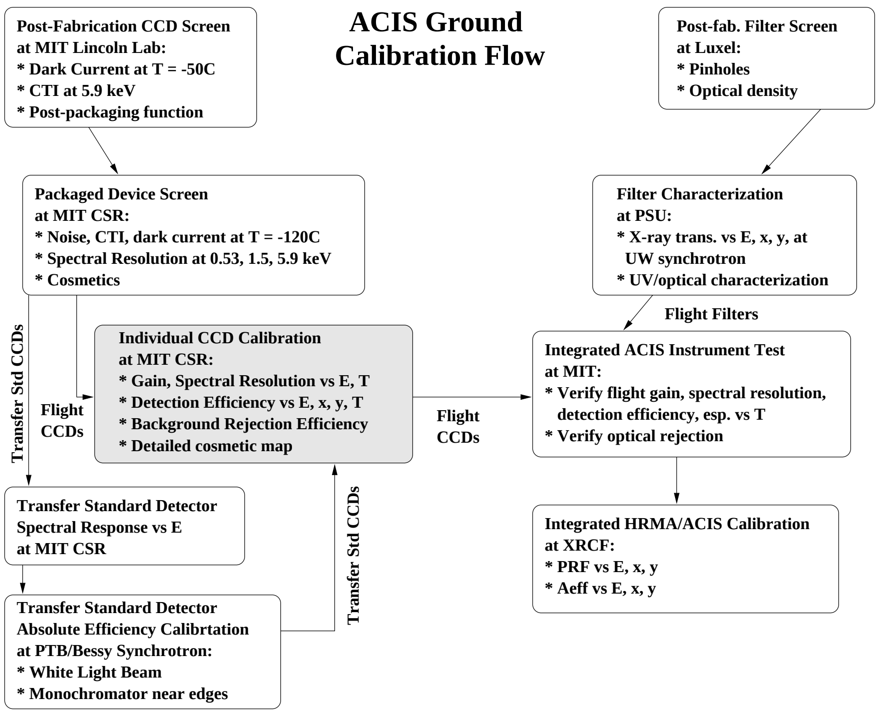

Figure 2: ACIS ground calibration flow. This paper focuses on the measurements listed in the shaded box.

This strategy is recapitulated at the ACIS instrument level: various instrument subsystem models are calibrated, and then checked during instrument-level performance tests. This structure is illustrated in Figure 2. The selection and calibration of individual ACIS CCD detectors is shown on the left half of Figure 2. Following fabrication at MIT Lincoln Laboratories, devices are subjected to a two-stage screening process, which is described in greater detail by Pivovaroff et al.[4]

The remainder of the CCD subassembly calibration is divided into two phases. A subset of flight-quality devices has been characterized as transfer standards at the facilities of the Physikalisch-Technische Bundesanstalt (PTB) Laboratory at the Berliner Electronenspeichering-Gesellschaft für Synchrotronstrahlung (the BESSY synchrotron storage ring). The intensity of the undispersed synchrotron radiation at the PTB beamlines can be calculated to high accuracy (better than 1% in the spectral band 0.2 - 4 keV).[11] This radiation provides a primary standard for the absolute detection efficiency calibration of the transfer standard CCDs. 4 keV, we plan to use a Si(Li) detector as a transfer standard. This device and its use in ACIS CCD calibration are discussed by Manning et al.[7] We do not discuss it further here.

The calibration of flight detectors is performed at the MIT Center for Space Research. As is indicated in Figure 2, these measurements include determination of the energy-to-pulse-height relationship, the spectral resolution, and higher moments of the spectral response function. Dependence of the spectral response function with detector temperature, detector clock levels, and readout mode is also measured. Detection efficiency, especially as a function of position on the detector, is measured with reference to the calibrated transfer standard CCD detectors. Various other pertinent detector performance characteristics, as listed in Figure 2, are also measured.

Following subassembly calibration of individual CCDs, the detectors will be installed on the flight focal plane, which will then be integrated with the instrument electronics and other ACIS components. Key among these, from a calibration standpoint, are the ACIS optical blocking filters, which have been calibrated separately by our colleagues at the Pennsylvania State University.[9,10] The integrated ACIS instrument will be tested to verify selected aspects of the the subassembly calibration. Following the integrated instrument test, ACIS, along with other AXAF science instruments, will be calibrated with the AXAF High-Resolution Mirror Assembly at NASA's X-ray Calibration Facility (XRCF) at Marshall Space Flight Center.

The remainder of this paper describes the most important aspects of the CCD subassembly calibration listed in the shaded box in Figure 2: the spectral response characterization and the detection efficiency measurements.

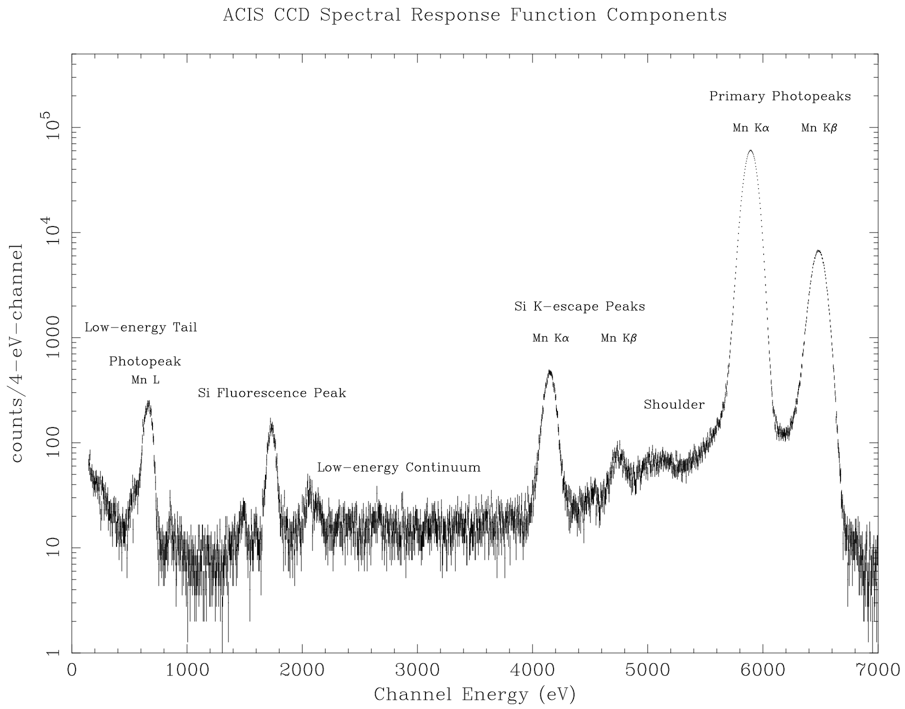

Figure 3: Principal components of the CCD spectral response function. The (asymmetric) primary photopeaks, silicon K-escape and fluorescence features, and the extended low-energy tail are indicated. Note that the upturn in the tail at very low energies (E< 400 eV) is not due to electronic noise, but is a characteristic of the detector itself.

4 Spectral Response Function Calibration

4.1 Objectives and Assumptions

A typical CCD spectral response function is illustrated in Figure 3. This pulse-height spectrum was obtained from a flight-candidate device using a radioactive Fe^{55} source, which produces characteristic K and L X-rays of Mn at 5.9, 6.4 and 0.65 keV; only events in which the charge is confined to precisely one or two pixels (so-called one- and two-pixel events) are included in the histogram. The various parameters to be constrained by the spectral response function measurements are indicated in the figure. These include the location and asymmetric shape of the primary photopeak, the magnitude of the Si K-escape and fluorescence features, and the amplitude and shape of the extended low-energy tail. For the spectrum shown, about 2.5 % of the events occur outside of the primary photopeaks. The magnitude of the various features of the spectral response function depend on a variety of parameters, including X-ray energy, detector operating temperature and bias levels, and event selection criteria.

The objective of the spectral response function measurements is to constrain the various response function components as functions of these parameters. The specific accuracy objectives of the measurements are as follows:

i) Determine the energy scale (that is, the relationship between input X-ray energy, in eV, and photopeak location, in engineering units) with an error less than 0.1%, and line full-width at half maximum (FWHM) with an error less than 5%.

ii) Determine magnitude secondary peak features (Si K-escape, Si-K fluorescence) to 0.3% of total flux.

iii) Determine the magnitude of the low-energy tail with an accuracy 0.5% of main peak (error in integrated tail area : integrated main peak flux).

Some details of the spectral response function measurements made for nominal operating conditions are listed in Table 1. Reflection-grating spectrometers are used to sample the response function nearly continuously with incident energy below 2 keV. Discrete characteristic lines are used at higher energies. The apparatus used to make these measurements are described in other contributions to these proceedings.[5,6]

Note that each ACIS CCD contains four output amplifiers, and each of these amplifiers serves one (rectangular) quadrant of the device. Table 1 lists the number of counts obtained for each CCD quadrant.

System	Energy or Band (keV)	Total Counts (/energy/quad/ccd)
HIREFS Spectrometer	0.2-1.5	2×10^6 per band
HEXS	1.489 (Al-K) 2.622 (Cl-K) 6.404 (Fe-K) 9.886 (Ge-K)	6×10^5 per energy
	4.952 (V-K) 6.930 (Co-K) 7.478 (Ni-K) 8.639 (Zn-K)	6×10^5 per energy
Si Edge Spectrometer	1.0-2.2	5×10^5 per band

Table 1: Spectral Response Function Measurements

4.2 Sample results from spectral response function measurements

In this section we present sample results from preliminary analyses of spectral response function measurements made to date. The most fundamental parameters of the spectral response function are its first two moments (energy scale and spectral resolution), and we confine our discussion here to these characteristics. Results for one flight-quality device are shown in Figures 4 and 5. These data were obtained using the source described in these proceedings by Jones et al.[5] Measurements energy scale and spectral resolution are also made at lower energies as part of the ACIS CCD calibration. Results of these measurements are not reported here, but are discussed by Prigozhin et al.[6]

The energy scale measurements shown in Figure 4 indicate that, at energies between 500 eV and 10 keV, a linear energy scale is remarkably accurate: the RMS residual from the best-fit linear model is 3.6 eV. Note that one- and two-pixel events were selected in analyzing these data. The error bars shown on the residuals in the lower panel of the figure, at ± 2 eV, are far larger than the statistical precision of the peak centroid determinations. We believe that these error bars are a conservative estimate of the systematic errors inherent in the use of a simple, single-Gaussian model of the photo peak. Given these errors, the formal, 90% confidence error limits for the slope are $\pm 0.05\%$ of the mean slope.

The residuals exhibit a systematic trend with energy which remains to be investigated. A number of processes are expected to contribute to non-linearity in the CCD energy scale. These include the variation of charge collection efficiency with X-ray energy, and, especially at low energies, the variation of the mean ionization energy. [12] Qualitatively, the former effect contributes to negative residuals (in Figure 4) at high energies, while the latter effect may contribute to negative residuals at low energies. [12–14] We expect that accurate modelling of these effects, particularly with reference to charge collection efficiency, will improve our knowledge of the ACIS energy scale.

Figure 5 shows measured spectral resolution, expressed as full-width-at-half-maximum (FWHM) of the photopeak, for the same device, and the same data selection criteria, used for the measurements shown in Figure 4. A simple model of the form

$$FWHM(eV) = 2.35 \times g \times \sqrt{\sigma_{read}^2 + (E \times \frac{F \times w}{g^2})} \quad (1)$$

was fit to the data. Here g, the slope of the energy scale, in eV/adu, is a fixed parameter determined from the data in Figure 4, and E is the photon energy, in eV, F is the Fano factor and w is the mean ionization potential per electron-hole pair. (An "adu" is an analog-to-digital engineering unit for the energy scale.) The parameters varied in the fit are σ_{read}, the RMS system noise, expressed in adu, and the ratio $r = Fw/g^2$.

The best fit values for the model parameters are indicated in Figure 5. The best-fit value for the system noise is the equivalent of 2.4 electrons, RMS, which is consistent with the source-free measurements of this parameter. The best-fit value $r = 2.98 \pm 0.01 \times 10^{-2}$ (90% confidence error limits) implies, for example, that if $F = 0.12$, then $w = 4.08 \pm 0.01 eV/e^-$, which is significantly higher than the value $w = 3.73 eV/e^-$ reported by Lechner and Strueder.[12] On the other hand, the RMS residual deviation of the model from the data is 2.5 eV, which is much larger than errors due to counting statistics, which are expected to be about 0.3 eV RMS. Moreover, Figure 5 clearly shows that the residuals vary systematically with energy. These systematics must be understood before these data can support conclusions about fundamental physical parameters.

A number of processes must be accounted for to provide a more accurate prediction of ACIS spectral resolution as a function of energy. Probably the most important among these is the effect of incomplete charge collection on the shape and width of the photopeak. It is interesting to note that, at these very low system noise levels, the additional read-noise penalty incurred in reconstructing multiple pixel events is *not* a large contributor to spectral resolution. This is so because at low energies, where the multi-pixel noise penalty would significantly affect resolution, the proportion of multi-pixel events is quite low. At higher energies, the stochastic fluctuations in the photo-ionization process dominate the spectral resolution. In fact, for ACIS detectors operated with ACIS electronics, the resolution penalty from reconstruction of two-pixel events is less than 1%, in the FWHM, at all energies in the AXAF band. Partly for this reason, the naive model presented here predicts ACIS spectral resolution with an accuracy of order 5% in the FWHM.

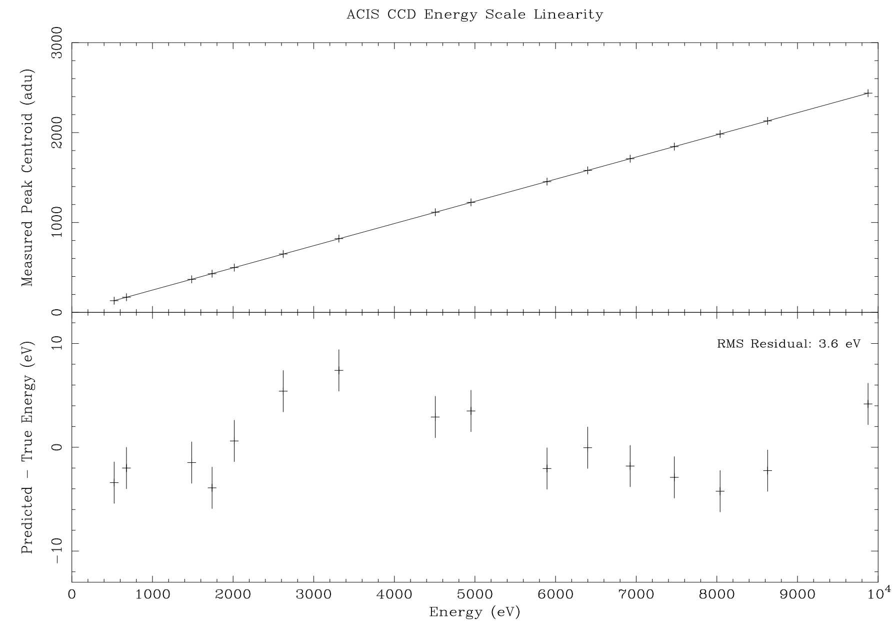

Figure 4: ACIS CCD energy scale linearity. The upper panel shows measured photopeak centroid is shown as a function of energy. The data set contains only one- and two-pixel events, and the single-Gaussian model neglects known asymmetries in the peak shape (see Figure 3.) The errors are much smaller than the size of the points shown in the upper panel. The solid line shows the best-fit linear energy scale relation. The lower panel shows residuals from the best-fit linear energy scale, expressed in eV, with ±2 eV error bars. The RMS deviation from the best-fit energy scale is 3.6 eV, or about 1 pulse-height channel.

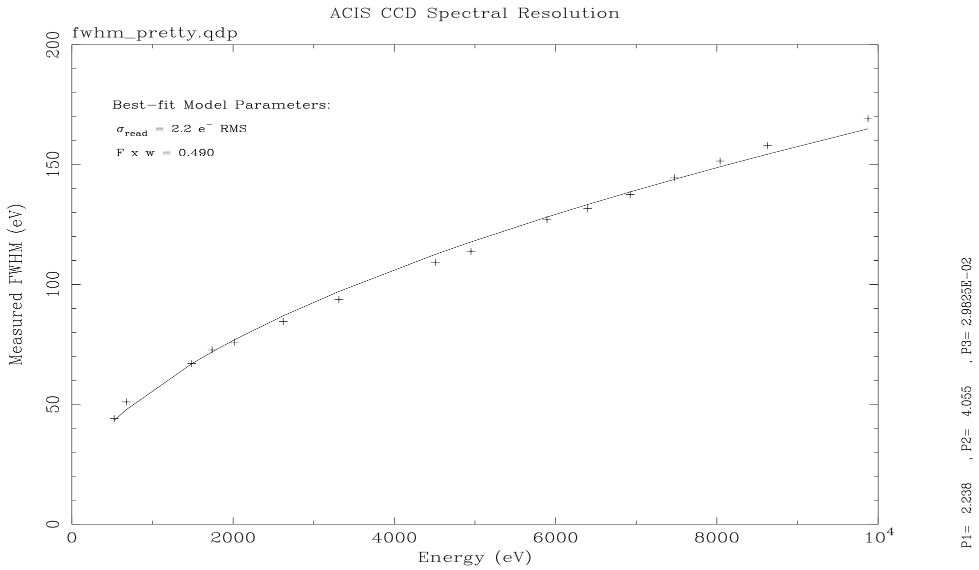

Figure 5: Measured ACIS CCD spectral resolution as a function of energy for the same device illustrated in figure 4. The full-width at half maximum (FWHM) of the photopeak was derived from a single-Gaussian fit to pulse-height spectra. Error bars are ± 0.3 eV for all points, and reflect the repeatability of the measurements.

5 Quantum Efficiency Measurements

5.1 Objectives and Approach

The objective of ACIS quantum efficiency measurements is to determine detector quantum efficiency as a function of X-ray energy with a statistical error less than 1% in each 32-pixel by 32-pixel detector subarray. The subarray size, which is just over 0.75 mm square, is dictated by the operational capabilities of the AXAF Observatory. In flight, the spacecraft attitude control system will be commanded to "dither" the telescope line of sight so that the image of a point source moves over a detector region of about this size. Knowledge of both photon detection times and the attitude history of of the spacecraft during this process will be used to recover the full angular resolution of the Observatory in spite of the dither.

Since there are 10^3 such cells per detector, to meet this objective at a single energy requires detection of at least 10^7 photons. Of course, it is neither practical nor necessary to make measurements of this accuracy as a continuous function of energy in the AXAF band. Instead, the detection efficiency measurement program has been designed to constrain parameters of a physical model of CCD detection. Very broadly, the detection model accounts for i) the probability that an incident X-ray will interact in the detector and ii) the probability that the charge packet produced by an interaction will be classified as an acceptable X-ray event. We find it convenient to use the term "branching ratio" to describe the latter probability.

The principal characteristics of the front-illuminated detector quantum efficiency are illustrated in Figure 6. The figure shows a best-fit model quantum efficiency as a function of energy (in this case for 1- and 2-pixel events) for an ACIS reference detector. The low-energy roll-off in detection efficiency, and the two prominent absorption features at 0.5 keV and 1.8 keV, are produced by oxygen and silicon in the CCD gate structure, which comprise a deadlayer. The roll-off in the efficiency at high energies is due in part to the decrease of the interaction probability in the depleted, photosensitive volume of the CCD. The branching ratio also falls as energy increases because the mean photon interaction depth increases with energy. Charge diffusion therefore tends to produce more extended charge clouds, and lower charge collection efficiency, at larger energies. An interesting exception to this trend occurs at the silicon K edge, where the sudden change in the mean interaction depth produces a corresponding change in the branching ratio. In this case, the change in branching ratio tends to compensate for the change in transparency of the dead layer.

The interaction probability model is a straightforward accounting of the geometry of the device, and (except near absorption edges) relies on well-established mass absorption coefficients. The model parameters to be constrained by the quantum efficiency measurements are essentially areal densities of the known dead-layers and photosensitive volumes of the detector. The probability of event acceptance depends on the details of event charge distributions since the event selection criteria depend on the spatial distribution of charge detected for each event. Although we plan ultimately to attempt to relate the measured branching ratios to a physical model of charge diffusion, we have have elected to characterize the branching ratios empirically in this preliminary analysis of the data.

Quantum efficiency measurement energies are listed in Table 2. These energies were selected on the basis of simulations of the model detector response which showed the sensitivity of the detector quantum efficiency to various deadlayer thicknesses. The energies chosen provide a wide energy baseline and bracket the most significant edges (those due to oxygen and silicon) in the CCD response.

System	Energy Range (keV)	Total Counts (/energy/ccd quad.)
Tritium (BI only)	0.277 (C-K)	2.5×10^6
Tritium	0.525 (O-K) 0.677 (F-K)	2.5×10^6
HEXS	1.740 (Si-K) 2.014 (P-K) 4.511 (Ti-K) 5.899 (Mn-K) 8.048 (Cu-K)	2.5×10^6

Table 2: ACIS CCD Quantum Efficiency Measurements

5.2 Reference Detector Calibration

As is indicated in Figure 2, ACIS CCD quantum efficiency measurements are made in two phases. First, selected, flight-quality CCDs are calibrated absolutely with respect to synchrotron radiation (both undispersed and dispersed) of calculable intensity. We have used the facilities of the PTB Laboratory at BESSY for this purpose. The detectors calibrated at the synchrotron then serve as the reference standards with respect to which the flight detectors are calibrated.

A detailed discussion of the calibration of the reference detectors will be presented elsewhere; we simply summarize the method here, and provide illustrative results. The technique is similar to one used by Scholze and Ulm [15] to calibrate a Si(Li) detector. The basic premise is that the spectral energy distribution of the undispersed synchrotron radiation can, under appropriate conditions, be calculated with high accuracy from first principles. These conditions have been realized sufficiently well at the PTB Laboratory at BESSY[11] that uncertainties in the calculated flux can be reduced below 1%. If the spectral redistribution function of the CCD is sufficiently well-understood, then the response of the detector to the undispersed synchrotron radiation can be used to determine the parameters of the detector deadlayer. A secondary benefit of the synchrotron radiation is that the spatial variation of flux can be calculated, so the data may be used to constrain spatial variations in detector efficiency. In order to make use of the synchrotron radiation without saturating the CCD detector, it is necessary to operate the electron storage ring at extremely low current (literally a few to a few dozen electrons in the storage ring).

To illustrate the quality of the data that can be obtained with this technique, Figure 7 presents a measured pulse-height spectrum obtained at PTB, together with the response predicted by the best-fit model. The deviations of the model from the data are shown in the lower panel. The RMS deviation, as a fraction of the data, is 1.6% for this fit. The response model assumes that the gate structure is of piece-wise uniform thickness, while the real gate structure thickness varies from phase to phase. Some detector model parameters, such as the CCD depletion depth and channel stop dimensions, were held fixed at nominal values in this fit. As is shown in table 3, the best-fit mean deadlayer thicknesses agree well with scanning electron micrograph measurements of sibling devices. The best-fit overall normalization of the predicted spectrum agrees, within 1.4%, with the predicted flux.

Gate Structure Parameter	Best-fit to Synchrotron Spectrum	Expected Value(s)
Si Gate Thickness	273 nm	227, 261, 324 nm
Si O_2 Thickness	275 nm	215, 300, 408 nm
Si_3 N_4 Thickness	27 nm	25-45 nm
Model Normalization	1.014	1.000

Table 3: Results of fits to synchrotron radiation spectrum

5.3 Relative Detection Efficiency Measurements

We measure the detection efficiency of the flight CCDs, relative to the synchrotron-calibrated standard detectors, using apparatus described by Jones et al. .[5] Briefly, both flight and reference detectors are illuminated by a quasi-monochromatic, temporally stable, diffuse (spatially uniform) X-ray beam of selectable energy. Since different physical processes are used to produce the X-rays at different energies, the spectral purity and spatial uniformity of the beam vary from energy to energy. Our use of CCD reference detectors, which have spectral and spatial resolution comparable to the flight devices being calibrated, allows us to measure and monitor the beam pattern and spectral content. This capability minimizes systematic errors resulting from non-ideal source characteristics.

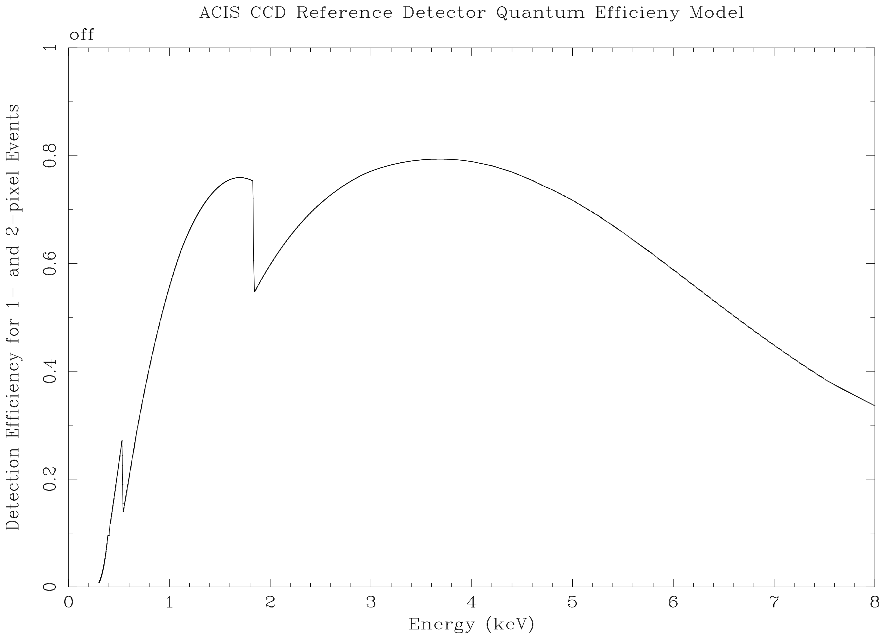

Figure 6: Best-fit Model Detection Efficiency for ACIS CCD Reference Detector

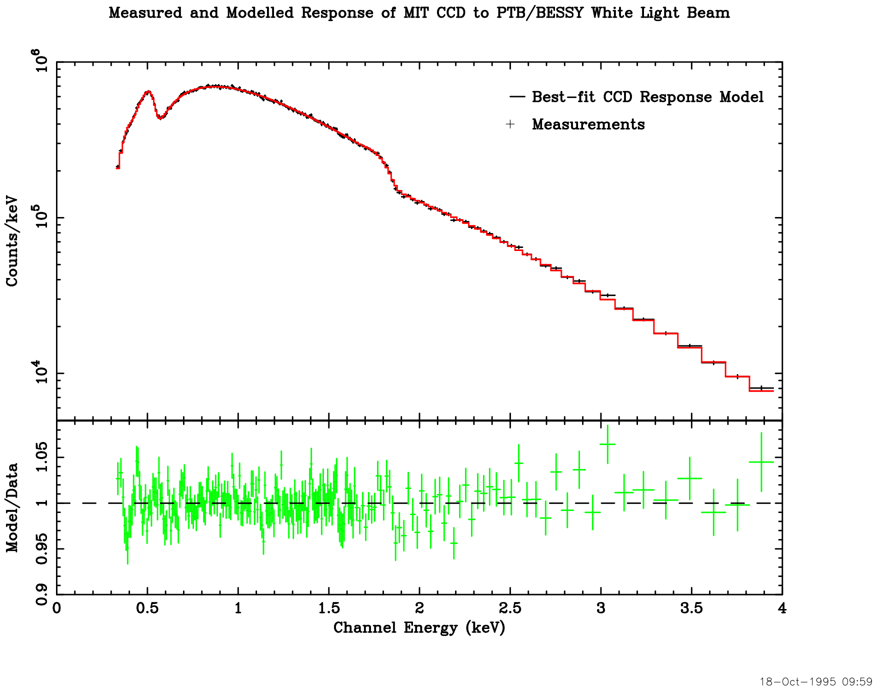

Figure 7: Response of an ACIS reference CCD to synchrotron radiation (crosses) with response predicted by the best-fit detector model. The lower panel shows the ratio of the model to the data. The RMS deviation of fit is 1.6%.

Some statistics of the relative detection efficiency measurements for one flight candidate detector (the same detector that was discussed in section 4) are shown in Table 4 for several energies. In this case, the flight detector efficiency is slightly lower than that of the reference detector at low energies; a reasonable fit to the low-energy (E< 3keV) data is obtained if the silicon-dioxide deadlayer is 0.11 ± 0.03 microns thicker on the flight device than on the reference detector. Such a difference between the flight and reference detectors is plausible,since the two detectors were produced in different lots (the flight detector is serial number w201c3; the reference detector is serial number w102c3). The flight detector has higher efficiency than the reference detector at higher energies because the flight detector is operated with higher bias than the reference.

Energy (eV)	Spatial Average Relative QE (Full Chip)	Variation of Relative QE, 32x32-pixel cells		
		RMS	Max.	Min.
525	0.890	0.019	0.964	0.827
677	0.780	0.020	0.865	0.725
1740	0.986	0.018	1.04	0.894
2014	0.951	0.017	0.993	0.877
5899	1.121	0.022	1.192	1.024

Table 4: Quantum Efficiency and Spatial Uniformity of an ACIS Flight CCD Relative to a CCD Reference Detector

Figure 8 illustrates the response uniformity of this flight candidate detector at 5.9 keV; this variation is typical of what is observed at other energies. Each pixel in the figure represents the normalized detection efficiency of a 32-by-32 pixel cell in the CCD, relative to the reference detector. Approximately 10^7 photons were detected in each detector at each incident energy; the contribution of counting statistics to the relative error in each cell is 1.4%. (Ultimately we hope to improve our knowledge of the beam pattern sufficiently that the statistical error can be reduced to that contributed by the test detector alone, viz., 1% per cell). The grayscale in the figure spans $\pm 0.06\%$, black-to-white, relative to the mean.

At all energies, the RMS fluctuation is about 2% on the scales shown in Figure 8. Note that statistical fluctuations of order 1.4% are expected in these data sets. Inspection of Figure 8 shows that the spectral variations are not randomly distributed over the detector. At this preliminary stage of analysis, we cannot rule out the possibility that there remain systematic errors, at the 1% level, in the flattening procedure. We believe we have demonstrated, however, that the detector response non-uniformity, over the spatial scales of interest, is at most of order 2%.

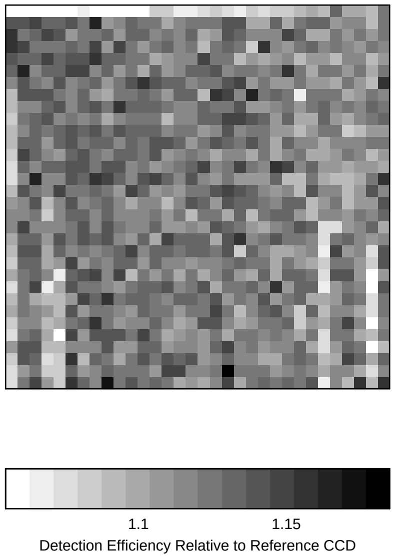

Figure 8: Spatial uniformity of detection efficiency for an ACIS flight CCD at 5.9 keV. Each cell in this figure is the mean efficiency of a 32x32 pixel subarray in the detector, measured relative to the reference detector. The grayscale spans ± 3 standard deviations about the mean.

6 SUMMARY

We have reviewed the strategy for ACIS CCD calibration, described the basic measurement objectives, and presented sample preliminary results from the calibration program. We believe our extensive calibration data set to be of high quality, and expect that through further analysis we will be able to achieve our ambitious goals for ACIS calibration accuracy.

7 ACKNOWLEDGMENTS

ACIS CCD calibration has required intensive effort by many people. The ACIS engineering team provided superb technical support for our calibration facility equipment and low-noise electronics. We acknowledge Beverly Fergason of MIT CSR for coordinating the data acquisition. Paul Plucinsky, Kenny Glotfelty and Norbert Schulz of the AXAF Science Center helped acquire, evaluate and archive the data. Kaori Nishikida and Catherine Grant of the Pennsylvania State University and Alesha Estes of the AXAF Science Center assisted with data acquisition and analysis. This work was supported by NASA contract NAS8-37716.

8 REFERENCES

[1] M. Weisskopf, S. O'Dell, R. Elsner and L. Van Speybrock, Proc. SPIE 2515, 312 (1995).

[2] G. Garmire, G. Ricker, M. Bautz, B. Burke, D. Burrows, S. Collins, J. Doty, K. Gendreau, D. Lumb and J. Nousek, Proc. AIAA Space Programs and Technology, Huntsville, Al., (March 1992).

[3] B. Burke, R. W. Mountain, P. J. Daniels, M. J. Cooper, V. S. Dolat, CCD soft x-ray imager for ASCA and AXAF, Proc. SPIE, 2006, 272 (1993).

[4] M. Pivovaroff, S. Kissel, M. Bautz and J. Woo Proc. SPIE 1996 (this conference).

[5] S. Jones, M. Bautz, S. Kissel and M. Pivovaroff, Proc. SPIE 1996 (this conference).

[6] G. Prigozhin, M. Bautz, K. Gendreau and G. Ricker, Proc. SPIE 1996 (this conference).

[7] H. Manning , S. Jones, S. Kissel, M. Bautz and G. Ricker, SPIE 1996 (this conference).

[8] T. Markert, C. Canizares, D. Dewey, M. McGuirk, C. Pak and M. Schattenburg, Proc. SPIE 2280, 168 (1994)

[9] L. Townsley, F. Powell, J. MacKay, M. Lagaly, J. Nousek and G. Garmire, Proc. SPIE (1996) this conference.

[10] G. Chartas, G. Garmire, J. Nousek, L. Townsley, F. Powell, R. Blake and D. Graessle, Proc. SPIE 1996 (this conference)

[11] D. Arnold and G. Ulm, Rev. Sci Instr. 63,1 (1992).

[12] P. Lechner and L. Strueder, Nuclear Instruments and Methods in Physics Research A, 354 464 (1995).

[13] R. Alig, S. Bloom and C. Struck, Phys Rev. B 22, 5565 (1980)

[14] G.W. Fraser et al., Nuclear Instruments and Methods in Physics Research A, 350, 368 (1994).

[15] F. Scholze and G. Ulm, Nucl. Instr. and Meth. in Phys. Res. A, 299, 354 (1990).